Seismic stimulation for enhanced oil recovery

Steven R. Pride (LBNL), Eirik G. Flekkøy, and Olav Aursjø

ABSTRACT

The pore-scale effects of seismic stimulation on two-phase flow are modeled numerically in random 2D grain0pack geometries. Seismic stimulation aims to enhance oil production by sending seismic waves across a reservoir to liberate immobile patches of oil. For seismic amplitudes above a well-defined (analytically expressed) dimensionless criterion, the force perturbation associated with the waves indeed can liberate oil trapped on capillary barriers and get it flowing again under the background pressure gradient. Subsequent coalescence of the freed oil droplets acts to enhance oil movement further because longer bubbles overcome capillary barriers more efficiently than shorter bubbles do. Poroelasticity theory defines the effective force that a seismic wave adds to the background fluid-pressure gradient. The lattice-Boltzmann model in two dimensions is used to perform pore-scale numerical simulations. Dimensionless numbers (groups of material and force parameters) involved in seismic stimulation are defined carefully so that numerical simulations can be applied to field-scale conditions. Using the analytical criteria defined in the paper, there is a significant range of reservoir conditions over which seismic stimulation can be expected to enhance oil production.

INTRODUCTION

The hope of seismic stimulation is that in a declining oil reservoir, seismic waves sent across the reservoir can cause oil production to increase. Quite literally, the idea is to shake the stuck oil loose and get it flowing again toward production wells.

Because oil reservoirs are often at kilometers or more of depth, it is common practice to use a downhole seismic source in a dedicated stimulation well. An often-used source is one that compresses then rapidly releases borehole fluid over a small depth range of the well. This creates seismic waves at relative proximity to the oil reservoir.

Our analysis suggests there is no need for this source to inject water into the formation, as sometimes is assumed. One should use the most powerful seismic source available and place it as close as possible to the reservoir.

Beresnev and Johnson (1994) provide a review of field evidence for and possible physical mechanisms behind seismic stimulation. On the theoretical front, Hilpert et al. (2000), Iassonov and Beresnev (2003), Beresnev et al. (2005), Beresnev (2006), and Hilpert (2007) give analytical models for how a single bubble stuck in a capillary tube might be mobilized if the capillary walls are shaken by a passing sound wave. Analysis or simulations for more realistic pore geometries and oil distributions are not available.

Laboratory evidence of seismic stimulation is rather limited. Roberts et al. (2001) performed laboratory experiments on cylindrical sand packs (5-cm diameter by 50-cm length) saturated with water and small amounts of TCE (a dense nonaqueous phase liquid at several percent volume fraction in the sand column). With water steadily flowing through the sand pack, axial time-harmonic (10- to 100-Hz) displacements were applied to one end of the sand pack, and the other end was clamped. TCE production increased significantly while time-harmonic stimulation was applied. To obtain an observable effect, the applied displacements needed to be greater than approximately 10 microns, which corresponds to seismic strain greater than 10^{-5}. In addition, TCE production increased as stimulation frequency decreased.

In a different laboratory study, Li et al. (2005) performed water flood experiments across a glass plate that had a rectangular network of grooves etched into the surface. At the start of each water flood, the grooves were filled completely with TCE. Floods were carried out with and without in-plane vibrations applied to the plate in the direction of the flood. Photography was used to monitor how the saturation levels of TCE decreased through time. Researchers observed that the rate of TCE production was enhanced when the acceleration amplitude of the vibrations was greater than 0.5 m/s^2 and when the frequency of vibration was less than 60 Hz. This corresponds to seeing a stimulation effect for a seismic-strain equivalent greater than approximately 10^{-5}. The point of the Li et al. (2005) experiments was to determine whether vibrational stimulation increases the rate

of production of the nonaqueous phase liquid (NAPL) during a water flood and not to determine whether stimulation can recover some fraction of the residual NAPL left behind after a water flood.

We will simulate numerically the effect of a passing seismic wave on the pore-scale two-phase flow. We use the lattice-Boltzmann model to perform the simulations and poroelasticity theory to define the effective forcing that the seismic wave adds to the background fluid-pressure gradient. Presently, simulations are done in two dimensions on cells that are typically 10×10 grains in size. However, extension to three dimensions and to larger systems is straightforward.

The simulation protocol is as follows: (1) Let the two immiscible fluids spontaneously separate with no external forces applied. (2) Turn on a background static pressure gradient and let both fluids flow until the nonwetting fluid (the oil) becomes stuck. (3) Turn on the seismic stimulation for several wave periods. (4) Then turn off the stimulation and see what new steady state emerges with only the background pressure gradient remaining. Over a significant parameter range, stimulation is observed to mobilize oil by causing coalescence of smaller droplets into bigger ones that flow more easily.

In the next section, we attempt to quantify the pertinent poroelastic effects of a passing wave. We keep only those effects of dominant importance. The arguments are based on 3D considerations of actual waves in real reservoirs. Subsequently, the appropriate dimensionless grouping of parameters and forces that control the mechanics of seismic stimulation are identified. This is essential in comparing numerical simulations to actual field conditions. Analytical conditions for stimulation to mobilize trapped oil also are given. Finally, the lattice-Boltzmann numerical simulations are discussed and presented. Despite the 2D nature of the simulations, we seek to draw conclusions concerning what types of reservoir conditions and seismic amplitudes are required for seismic stimulation to work.
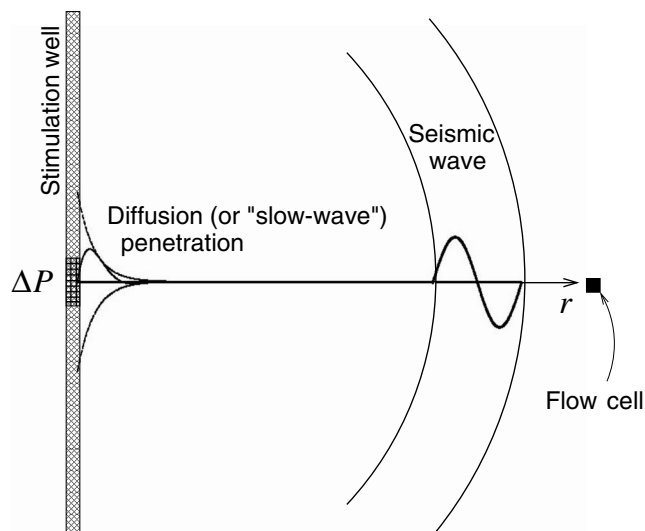

Figure 1. Schematic of applying a fluid-pressure perturbation ΔP over a certain depth range of a stimulation well with the goal of stimulating flow at points in the reservoir a distance r away. The seismic waves can deliver significant perturbation to a flow cell; however, the diffusional penetration from the borehole is totally negligible.

THE POROELASTICITY OF SEISMIC STIMULATION

General context of the problem

We imagine an oil reservoir being produced through the use of injection and extraction wells. Oil production in the field through time has fallen to low levels. Water is flowing, but much of the oil became effectively trapped when the water flood passed through. Such remaining oil patches (ganglia) might be present at economically significant volume fractions: Commonly, 30% or more of the pore space in a reservoir might be occupied by such trapped oil. We focus on an arbitrarily chosen small region within the reservoir that we call a "simulation" or "flow cell." Distribution of wells in the field is creating a net fluid pressure gradient $\mathbf{F}_o$ across this flow cell. However, any further details of the production wells are not required in what follows.

As proposed by Beresnev et al. (2005), an oil ganglion of downstream length h (typically much larger than grain sizes) becomes stuck when the downstream-pressure drop along the bubble hF_o just is balanced by a capillary-pressure increase $\sigma(1/R_{\text{down}} - 1/R_{\text{up}})$. Here, σ is the oil-water surface tension, and R_{down} and R_{up} denote the radii of curvature of the farthest downstream and farthest upstream menisci that bound the stuck bubble of oil. Throughout this work, water is taken as wetting the solid grains and oil as nonwetting. For the oil bubble to be trapped, either the downstream meniscus has a radius of curvature (multiplied by the cosine of the contact angle) greater than the radius of the pore-throat constriction through which it is trying to pass or the upstream meniscus has a radius of curvature (multiplied by the cosine of the contact angle) smaller than the main pore it is trying to enter. The goal of seismic stimulation is to displace these menisci enough that they can pass through their respective capillary barriers and begin to flow again under the background force F_o. Subsequent linking up with other bubbles to make longer and more efficiently transported bubbles is shown here, by means of numerical simulations, to be a very important effect. Although we emphasize liberating stuck oil ganglia, seismic stimulation also can be useful in preventing ganglia from becoming trapped in the first place or, as seen in the experiments of Li et al. (2005) and our numerical results, as a means of enhancing oil production rate during primary production.

As illustrated in Figure 1, we assume a seismic source in a stimulation well located a distance r from a given flow cell under study. By perturbing the fluid pressure in this borehole over a certain depth range, we aim to perturb the flow in the distant cell, with the goal of enhancing oil flux across that cell. As shown in the following subsection, fluid exchanges between the stimulation well and the surrounding reservoir play no important role in enhancing the oil flow. The seismic waves are overwhelmingly responsible for any stimulation effect. Any oil ganglia that are trapped marginally (on the verge of moving by F_o alone) are susceptible to seismic stimulation.

Perturbing flow at a distant cell

For the purposes of this subsection, it is sufficient to neglect the two-phase flow and consider only a single fluid saturating the pore space. In this case, the Darcy flux $\mathbf{q}$ across a cell is governed by the Darcy law

$$\mathbf{q} = \frac{k}{\eta_f}\mathbf{F}, \qquad (1)$$

where k is the permeability of the cell, η_f is the fluid's viscosity, and **F** is the total effective-force driving flow (with units of a pressure gradient). This total force can be decomposed as

$$\mathbf{F} = \mathbf{F}_o + \Delta\mathbf{F}_o + \mathbf{F}_a, \qquad (2)$$

where $\mathbf{F}_o$ is the background (i.e., production) pressure gradient and $\Delta\mathbf{F}_o$ and $\mathbf{F}_a$ are created by changes in the stimulation well. If the pressure perturbation applied in the stimulation well has a component that is steady in time and if this well is perforated, there will be a static force perturbation $\Delta\mathbf{F}_o$ that simply adds to $\mathbf{F}_o$ to create a total static forcing coming from all wells in the region. By conservation of fluid mass, this $\Delta\mathbf{F}_o$ has an amplitude that falls off with distance r as $1/r^2$; specifically, for a homogeneous reservoir, one has

$$\Delta F_o = \frac{\eta_f \Delta Q_o}{k4\pi r^2} \qquad (3)$$

where ΔQ_o is the perturbed volumetric flow rate across the perforated portion of the stimulation well.

Force F_a is the amplitude of any time-harmonic forcing created by the fluid-pressure perturbations applied in the stimulation borehole. If this borehole is perforated, the time-harmonic forcing has contributions both from an oscillating fluid-pressure diffusion that sometimes is called the Biot slow wave (Biot, 1956) and from a propagating seismic wave (see Figure 1). The diffusional contribution has a spatial falloff dominated by a factor $e^{-r/d}$, where the diffusive skin depth d is given by $d = \sqrt{D/\omega}$ with D the fluid-pressure diffusivity given by $D = kM/\eta_f$. The fluid-storage incompressibility M, to an excellent approximation (Pride, 2005), is given by $M = K_f/\phi$, where K_f is the fluid's bulk modulus and ϕ is porosity. Using values for a highly permeable sandstone saturated with water ($k = 10^{-12}$ m², $\phi = 0.2$, $K_f = 2\times10^9$ Pa, $\eta_f = 10^{-3}$ Pa s), one then obtains $D = 10$ m²/s as almost an upper bound for the diffusivity in rocks. So for all frequencies $f = \omega/2\pi > 10$ Hz, which correspond to the seismic frequencies of interest here, the skin depth is far less than a meter. Thus, the diffusive contribution to F_a is always completely negligible for flow cells more than a meter from the stimulation borehole.

Thus, the principal contribution to F_a is coming from the seismic wave, which (apart from a small loss because of intrinsic attenuation) is conserving energy as it propagates outward spherically. Energy conservation requires the energy density in the wave to fall off with distance as $1/r^2$, and because the energy density is proportional to the strain squared, the strain must fall as $1/r$. The wave-induced pressure gradient F_a goes as the strain multiplied by an elastic modulus and divided by the wavelength and thus also falls off as $1/r$. We conclude that because a static (DC) perturbation has a fluid force ΔF_o falling as $1/r^2$ (although the seismic perturbations have fluid forces F_a falling as $1/r$), it might be more cost-efficient to use a stimulation well as a source of seismic waves than as a means to perturb the steady background driving force. Therefore, ΔF_o will be set to zero, and F_a will represent exclusively the acoustic (seismic) force perturbations.

Finally, because it has been shown that seismic-wave forcing dominates over the slow wave for all distances $r > 1$ m from the stimulation well, the well need not be perforated, i.e., fluid exchanges between the stimulation well and the reservoir can be neglected entirely. However, because a perforated well lining is less stiff than a nonperforated lining, the seismic coupling between borehole and

Symbol	Meaning
A	Lattice-Boltzmann interface parameter
B	Skempton's coefficient when both fluids are in the pores
B_f	Skempton's coefficient when fluid f is in the pores
c_p	Seismic P-wave velocity
c_s	Seismic S-wave velocity
Ca	Capillary number
d	Skin depth of pressure diffusion
D	Fluid-pressure diffusivity
f	Frequency in Hertz
F_o	Background (steady) pressure gradient
F_a	Seismic-force perturbation
ΔF_o	Steady-force perturbation
G	Shear modulus of rock
h	Downstream length of a stuck oil bubble
j_{oil}	Flux of oil
k	Permeability
K_d	Drained bulk modulus
K_f	Bulk modulus of fluid f
K_s	Bulk modulus of grain material
K_u	Undrained bulk modulus
ℓ	Hydraulic throat radius
M	Fluid-storage incompressibility
N	Number of lattice points to each side
p_f	Wave-induced fluid-pressure increment
q	Darcy flow velocity
r	Distance from seismic source
R	Reynolds number
R_{down}	Downstream meniscus radius
R_{up}	Upstream meniscus radius
S	Stimulation number
S_m	Surface area of the menisci
t	Time
T	Dimensionless frequency number
$\mathbf{u}$	Displacement of solid grains
U_c	Characteristic flow speed
v_f	Volume fraction of fluid f
V_{oil}	Specific volume of oil produced
β	Interface angle in the lattice-Boltzmann model
η_f	Shear viscosity of fluid f
λ	Lattice-Boltzmann collision parameter
ρ_f	Mass density of fluid f
ρ	Mass density of bulk rock
σ	Surface tension
θ	Wave strain
Θ	Contact angle
ω	Circular frequency

Seismic forces driving relative flow

A typical seismic wavelength is always much larger than the size of the flow cells under consideration. The seismic band of frequencies over which it is relatively easy to propagate seismic energy is approximately 10 to 100 Hz. This corresponds to wavelengths ranging from approximately 100 to 10 m. The flow cells modeled here are smaller than a centimeter and are thus far smaller than a seismic wavelength.

As a wave traverses such a small cell, it creates an effective force $\mathbf{F}_a$ uniformly acting on the fluid that is moving in relative motion to the grains. This force consists of both a wavelength-scale pressure gradient and an apparent force arising from the fact that the reference frame for the flow (the framework of grains) is accelerating. These two contributions can be written as

$$\mathbf{F}_a = -\nabla p_f - \rho_f \frac{\partial^2 \mathbf{u}}{\partial t^2}, \tag{4}$$

where ∇p_f is the macroscopic pressure gradient acting across the flow cell, ρ_f is the fluid density, and $\mathbf{u}$ is the average displacement of the solid grains in the cell. The pressure gradient is present only in the case of a compressional wave. In the apparent force of the second term, the acceleration of the frame of reference is equivalent to a gravitational acceleration and occurs for both compressional waves and shear waves. This apparent force corresponds to what one feels when standing on a bus that accelerates.

To model the two force contributions in equation 4, we note that a seismic wavefront is effectively planar relative to the size of a flow cell when the distance r from the source to the cell is much larger than the size of the cell. For a time-harmonic plane wave moving in the x direction, the seismic strain θ acting on the bulk material goes as $\theta(x,t) = \theta_o e^{i\omega(x/c-t)}$, where c is the wave speed and θ_o is the strain amplitude (taken here to be independent of frequency over the range of frequencies considered).

For a compressional wave at 10 to 100 Hz, Pride (2005) has shown that the poroelastic response is effectively undrained, i.e., as much fluid enters the flow cell as leaves, so there is no net change in the fluid mass. In this case, the fluid-pressure increment p_f is related to the wave strain θ as $p_f = -BK_u\theta$, where K_u is the undrained bulk modulus and B is called Skempton's (1954) coefficient and is the ratio of pore-pressure change to confining-pressure change for undrained conditions. For liquid-saturated materials found in a sedimentary basin, one typically has $0.3 < B < 0.7$, with large values corresponding to softer materials. Expressions that detail how the undrained moduli K_u and B depend on the underlying fluid and solid moduli are given in Appendix A. Further, the seismic velocities at such frequencies are given as

$$c_p = \sqrt{\frac{K_u + 4G/3}{\rho}} \quad \text{and} \quad c_s = \sqrt{\frac{G}{\rho}} \tag{5}$$

for compressional waves and shear waves, respectively, where G is the shear modulus (which is independent of the fluid properties at seismic frequencies) and ρ is the average density of all the material in a flow cell.

For a compressional wave, the amplitude of the force driving relative flow is

$$F_a = -i\omega c \left[\rho_f + \frac{\rho B}{} \right] \theta \tag{6}$$

where the ρ_f term in brackets corresponds to the apparent force from the acceleration of the frame of reference and the ρB term corresponds to the fluid-pressure gradient force. This expression is the principal result of this section. As seen in Appendix A, when some gas is present in the system, B becomes negligibly small, and we are left with only the forcing from the acceleration. For liquid systems, the two terms are of comparable importance. For a shear wave, there are no compressional changes, and the effective force is simply $F_a = -i\omega\rho_f c_s\theta$, arising from acceleration of the framework of grains alone.

At the pore scale, these seismic forces can be taken as uniform body forces in the Navier-Stokes equation for the local relative flow in the pores. If the oil and water have significantly different densities ρ_f, one should formally require the apparent inertial force caused by acceleration of the grains $-i\omega\rho_f c_{p,s}\theta$ to be different in the oil and water phases. However, for most crude oils and pore waters, the density difference is on the order of 20% (with oil being lighter), which might reasonably be neglected in a first modeling of seismic stimulation. The macroscopic fluid-pressure gradient given by the ρB term in equation 6 is the same for oil and water phases.

Last, in addition to creating a pressure gradient across a flow cell, a compressional wave also tries to change the average pressure of each fluid in the flow cell. Because water is slightly less compressible than oil, the associated fluid-pressure equilibration will cause a displacement of the menisci from water patches toward oil patches. This effect is modeled in Appendix B, where it is determined to be negligible relative to the menisci displacements driven by the seismic forcing F_a of equation 6.

DIMENSIONLESS NUMBERS AND CONDITIONS NECESSARY FOR STIMULATION TO WORK

To perform numerical simulations pertinent to field experiments, the dimensionless groups that characterize seismic stimulation must be identified. As always, two flows will be similar if the dimensionless numbers are the same, even though some of the material properties, force amplitudes, or length scales are different in the two situations.

Oil and water have different viscosities, so their ratio η_{oil}/η_{water} must be one of the dimensionless groups. For crude oils, one commonly has $\eta_{oil}/\eta_{water} \gtrsim 10$.

The ratio F_a/F_o of seismic forcing to the background fluid-pressure gradient is another important dimensionless group. The pressure gradients used in oil-reservoir production are commonly on the order of a few kPa/m (e.g., tens of bars over 500 m). Combining this order-of-magnitude appropriate value for F_o with $|F_a| \approx \omega\rho_f c_p\theta$ and the properties $\rho_f = 10^3$ kg/m^3 and $c_p = 3000$ m/s gives the rough field estimate of

$$\frac{F_a}{F_o} \approx \frac{f}{10^{-4}\ \text{Hz}}\theta, \tag{7}$$

where $f = \omega/2\pi$ is frequency in Hertz. Therefore, a 10-Hz source delivering a strain of $\theta = 10^{-6}$ (a large but common seismic-strain level) to some flow cell corresponds to $F_a/F_o \approx 10^{-1}$, although a 100-Hz source delivering the same strain would yield $F_a/F_o \approx 1$.

However, it should be kept in mind that F_a falls with distance as $1/r$. If the wave strain is 10^{-5} at 10 m from the source position (stimulation well), it will be 10^{-6} at 100 m and 10^{-7} at 1 km. How F_o varies spatially is a function of how the production wells are distributed.

some regions between the injection and extraction wells where F_o is a spatial constant and other regions (marked with an X in Figure 2) where it falls even more rapidly than $1/r$. One can conclude that for downhole sources commonly available today, there will always be some parts of the reservoir for which $F_a/F_o > 1$. In their laboratory experiments, Roberts et al. (2001) measured an enhanced production of DNAPL as long as $F_a/F_o > 10$.

Any problem with viscous flow involves the Reynolds number R, which is the ratio of the nonlinear convective inertial force to the viscous shearing force. It is given by $R = \rho_f U_c \ell / \eta_f$, where ℓ is a characteristic pore size and U_c a characteristic flow velocity. We can use Darcy's law to identify a characteristic flow velocity $q = \phi U_c = (k/\eta_f)F_o$. Further, the characteristic pore size ℓ can be estimated from the permeability relation $k = (\phi\ell)^2$, which is meant to crudely characterize Thompson et al.'s (1987) 3D percolation estimate of $k = \ell^2/(226F)$, where F is the electrical formation factor and Archie's (1942) law states that $F = \phi^{-m}$, with $m = 2$ a realistic cementation exponent. This combines to give the estimate

$$R = \frac{\rho_f}{\eta_f^2} \frac{k^{3/2}}{\phi^2} F_o. \qquad (8)$$

Again, using the order-of-magnitude estimates of $k = 10^{-12}$ m², $\phi = 10^{-1}$, and $F_o = 10^4$ Pa/m gives the field estimate of $R \approx 10^{-3}$. This means that there is laminar and/or creeping flow throughout the reservoir. Our simulations need only to have $R \ll 1$ for them to be similar to the field situation in this regard.

Because menisci are present, the capillary number Ca needs to be specified. The capillary number is the ratio of a characteristic viscous shear stress $\eta_f U_c / \ell$ to a characteristic capillary pressure σ/ℓ and thus is given by $\text{Ca} = \eta_f U_c / \sigma$, where σ is the oil-water surface tension. Using the above estimate for U_c gives

$$\text{Ca} = \frac{kF_o}{\phi\sigma}. \qquad (9)$$

Again, using $k = 10^{-12}$ m², $\phi = 10^{-1}$, $F_o = 10^4$ Pa/m, and $\sigma = 10^{-2}$ Pa m gives a characteristic field value of Ca $= 10^{-5}$, which means that in the field, we are in a regime where capillary effects control the menisci displacements.

As discussed previously, for an oil droplet to be trapped (immobile) in the presence of the background pressure gradient F_o acting on it, one must have

$$F_o h = \sigma\left(\frac{1}{R_{\text{down}}} - \frac{1}{R_{\text{up}}}\right), \qquad (10)$$

where h is the length of a characteristic oil bubble and R_{down} and R_{up} are the radii of curvature of the farthest downstream and farthest upstream menisci that bound the bubble. The condition for an oil bubble to just break through a pore-throat constriction of radius ℓ blocking downstream migration is that

$$R_{\text{down}} = \frac{\ell}{\cos \Theta}, \qquad (11)$$

where Θ is the oil-water-solid contact angle. On inserting equation 11 into equation 10 and adding the acoustic forcing F_a to the background force F_o, the condition for seismic stimulation to mobilize a

$$(F_o + F_a)h > \frac{\sigma \cos \Theta}{\ell}\left[1 - \left(\frac{R_{\text{down}}}{R_{\text{up}}}\right)_c\right], \qquad (12)$$

where $(R_{\text{down}}/R_{\text{up}})_c$ is defined at the moment of breakthrough and is necessarily a fraction less than one. Instead of attempting an involved analysis of $(R_{\text{down}}/R_{\text{up}})_c$, we simply approximate it as $1/2$, which is consistent with observations from the lattice-Boltzmann simulations to follow.

In dimensionless form, a sufficient condition for stimulation to work is then

$$\frac{2F_o h \ell}{\sigma \cos \Theta}\left(1 + \frac{F_a}{F_o}\right) > 1. \qquad (13)$$

Using $\ell \approx \sqrt{k}/\phi$ as an estimate of the constricting pore radius and introducing a new dimensionless number S that we call the "stimulation number" allows the stimulation criterion finally to be written as

$$\frac{F_a}{F_o} > \frac{1}{S} - 1, \qquad (14)$$

where

$$S = \frac{2F_o h \sqrt{k}}{\sigma \phi \cos \Theta} = \frac{2\text{Ca}}{\cos \Theta}\frac{h}{\sqrt{k}}. \qquad (15)$$

We necessarily have that $S \gg \text{Ca}$. The closer S is to one, the closer the oil bubble is to getting through its bounding constriction and the smaller F_a/F_o must be for stimulation to work. If $S > 1$, the oil will flow under the background gradient alone. Nonetheless, even when $S > 1$, stimulation might act to push a slowly advancing bubble more rapidly through a constriction that is retarding its downstream progress. Thus, stimulation can enhance oil production even when $S > 1$, as will be seen in the numerical simulations.

The stimulation condition of equation 14 is based on a static-force argument. There is also a dynamic consideration — whether there is enough time in a half-cycle of time-harmonic stimulation for the bubble to advance through the constricting pore throat and become liberated. The distance δ_q that a meniscus advances in a half-cycle of time $1/(2f)$ where f is frequency in Hertz is given by $\delta_q = (\langle q_{\text{oil}}\rangle/\phi)/(2f)$. The oil's instantaneous filtration velocity is given by Darcy's law $q_{\text{oil}} = (k/\eta_{\text{oil}})F_a \sin(2\pi ft)$, which gives $\langle q_{\text{oil}}\rangle = (k/\eta_{\text{oil}})F_a/2$ when averaged over the first half of a cycle. Then identifying the distance the downstream meniscus must advance to get through the constriction as $\ell = \sqrt{k}/\phi$, yields the dynamic criterion
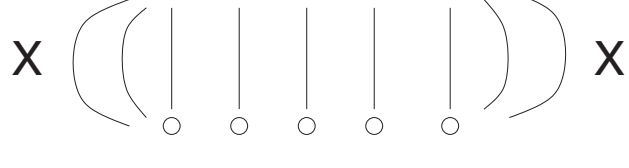

Figure 2. Map-view schematic of the possible positions of production wells in a reservoir along with the directions of pressure gradients $\mathbf{F}_o$ between them (solid lines). Solid dots indicate injection wells, and open circles represent extraction wells. In the fringe regions marked with an X, F_o will fall off rapidly with distance, al-

$$T = \frac{\ell}{\delta_q} = \frac{4f\eta_{\text{oil}}}{\sqrt{k}F_a} < 1. \qquad (16)$$

Both the static-force condition of equation 14 and the dynamic condition of equation 16 must be satisfied simultaneously if stimulation is to advance a stuck oil bubble through its bounding barrier.

When the stimulation-force amplitude F_a is set independently, the dimensionless number $T = 4f\eta_{\text{oil}}/(\sqrt{k}F_a)$ can be thought of as the dimensionless frequency. However, if the stimulation force F_a is given by the value appropriate for a seismic wave $F_a \approx 2\pi f c_p \rho_f \theta$, then T becomes independent of the wave frequency to the extent that seismic strain θ is independent of frequency.

Hilpert (2007) demonstrates that capillary-resonance effects are possible at sufficiently high frequencies. However, over the seismic band of frequencies of interest in the present study, these relaxations are not important in rocks or sediments.

Therefore, the suite of dimensionless numbers that must be specified for two seismically stimulated flows to be considered similar are $\eta_{\text{oil}}/\eta_{\text{water}}$, F_a/F_o, R, Ca, S, T, and v_{oil}, where v_{oil} is the volume fraction of oil in the system. Further, the conditions $F_a/F_o > 1/S - 1$ and $T < 1$ both must be satisfied for stimulation to mobilize trapped oil.

NUMERICAL SIMULATIONS

Two-dimensional lattice-Boltzmann modeling is performed as a means of numerically simulating the effects of a passing wave on the two-phase flow. As described in Appendix C, the lattice-Boltzmann model is formally equivalent to the Navier-Stokes equations controlling fluid flow and properly allows for the effects of surface tension and contact-line forces at the menisci that separate regions of immiscible fluids. The menisci are free to stretch and contact lines are free to migrate in the modeling. On either side of a moving contact line, no slip-flow conditions are maintained on the grain surfaces. The background production gradient F_o is modeled as a uniform force on both fluids, although the acoustically induced perturbations F_a are modeled as a uniform force that has a sinusoidal time dependence. Spatially varying fluid pressures develop in response to these applied forces. The simulations in no way make use of the two stimulation criteria of the previous section. Indeed, the numerical simulations are used as an independent test of the criteria.

Parameterization and protocol

All numerical simulations were performed using the following lattice-Boltzmann parameters (all parameters are given in units where the lattice constant and time step equal unity): number of lattice points to each side of a square modeling region $N = 128$, oil viscosity $\eta_{\text{oil}} = 0.1$, water viscosity $\eta_{\text{water}} = 0.02$, mass density per site $\rho = 3$, surface tension $\sigma \approx 0.3$, and seismic frequency $f = 0.001$. Because the acoustic force F_a is set independently and the Reynolds number is negligible, the mass density in the lattice-Boltzmann model is arbitrary. On selecting a mass density prior to simulation, viscosity is determined by the collision parameter λ of Appendix C, and surface tension is set by the interface parameter A of Appendix C. The permeabilities (in lattice units) of the various porous media considered are in the range of $k = [0.1, 0.5]$, and the porosities in these 2D simulations are in the range of $\phi = [0.5, 0.75]$. Such

will be connected across a sample only when $\phi \geq 0.4$. Permeability is measured numerically by applying a steady force to a single fluid phase.

The dimensionless numbers in the simulations are in the range of

$$R = [0.10, 0.14]$$
$$\text{Ca} = [1.5 \times 10^{-3}, 2.0 \times 10^{-3}]$$
$$T = [0.14, .19]$$
$$\eta_{\text{oil}}/\eta_{\text{water}} = 5. \qquad (17)$$

All simulations are run with $F_a/F_o = 1$ except for the graph (example) in which F_a/F_o is taken as the independent variable and the example in which $F_a = 0$. Further, the stimulation number S can vary between simulations and is not fixed a priori.

Comparing the simulation values of the dimensionless numbers to typical field values, we observe that $R < 1$ in both cases (laminar flow regime), which is the only requirement. The simulations have a capillary number that is approximately an order of magnitude larger than the estimated field value. The problem of using the field value of Ca in the simulations is linked to a well-known instability in the lattice-Boltzmann model (e.g., Rothman and Zaleski, 1997) that arises when the surface tension (or A parameter) in the simulations is chosen too high. At $\text{Ca} = 10^{-3}$, the simulations just are entering the flow regime where capillary forces dominate the viscous forces and, in this sense, are beginning to be similar to field conditions.

In all the present simulations, the background force is applied from left to right (the flow direction), although the top and bottom and left and right flow boundaries are periodic.

Some characteristic snapshots corresponding to various stages of the simulation protocol used in this study are given in Figure 3, and the associated average Darcy velocity of the oil during each stage is shown in Figure 4. The porous material in this demonstration example has $\phi = 0.5$ and $k = 0.5$ (again in lattice units). Further, the fraction of the pore space occupied by oil is 50% (with water occupying the other 50%).

The simulation protocol is the same for each production run presented in this article and is broken into the four time intervals denoted in both Figures 3 and 4. It is defined as follows: (1) Oil and water are allowed to separate spontaneously from an initial homogeneous distribution with all applied forcing set to zero. (2) The background force F_o then is applied uniformly to oil and water, initially causing some flow but often resulting (depending on both the value of F_o and the oil-volume fraction) in the oil becoming trapped on capillary barriers with an associated large decrease in the average Darcy velocity in the system. (3) Seismic stimulation then is applied (both $F_a \neq 0$ and $F_o \neq 0$). (4) Seismic stimulation is turned off with a new steady-flow state emerging under the influence of F_o alone. Only three seismic-wave periods of stimulation (which corresponds to approximately 10^{-1} s of stimulation in the field) ever are applied in our simulations. If, as in field applications, the stimulation is applied for many millions of wave periods, the effect on the total volume of produced oil necessarily will increase beyond what we have determined here.

The main pore-scale effect of applying the seismic stimulation is to mobilize the stuck oil droplets, which allows them to coalesce and form longer bubbles. As the criterion of equation 12 makes clear, longer bubbles have a greater applied pressure drop along them, which allows them to more easily overcome the capillary barriers

moving) prior to application of stimulation. In the final steady state that emerges once stimulation is turned off, a system-spanning steady stream of oil created by the wave-induced coalescence of the oil droplets can be observed.

Stimulation easily can create such system-spanning streams when oil occupies about 40% to 60% of the pore space. As the oil-volume fraction is increased, there becomes enough oil that the background force alone can create a system-spanning stream and oil never becomes trapped. As the oil-volume fraction is lowered, the likelihood of creating such a single-spanning stream, even with stimulation-induced mobilization and coalescence, is reduced progressively. To keep oil droplets moving at such lower oil-volume fractions, it is necessary to apply stimulation repeatedly. In real, 3D, nonperiodic systems, even if a system-spanning oil stream develops, it potentially will break up because of Rayleigh instability (Chandrasekhar, 1961). This is the 3D effect responsible for the pinching off of droplets at a slowly dripping faucet. Smaller bubbles thus created will become trapped again on capillary barriers, in which case repeated stimulation will be required.

Results for six materials

Next we focus on oil production in the six porous materials presented in Figure 5. The permeabilities and porosities of these materials are shown in the legend of Figure 6 and subsequent figures. In all examples presented here, oil occupies one-third of the pore space and water two-thirds. We conservatively chose this oil-volume fraction so that system-spanning oil streams were not created. When system-spanning streams are created, such as in Figures 3 and 4, stimulation can increase oil production greatly compared with the results presented here.

For each of the six porous materials studied, Figure 6 depicts the corresponding total oil production during an entire production run (the entire 18,000-time-step simulation) when no seismic stimulation is applied. The plotted quantity is the specific oil volume that we define as

$$V_{\text{oil}} = \int dt \bar{j}_{\text{oil}}, \qquad (18)$$

where j_{oil} is the local volume flux of oil (from left to right), $\bar{j}_{\text{oil}}$ is the spatial average of this flux over the entire simulation (flow) cell, and the time integral runs over the entire simulation time of 18,000 time steps. In steady state, the specific oil volume V_{oil} multiplied by the height of the simulation cell will converge to the volume of oil that crosses a surface perpendicular to the flow (the produced oil volume).

Figure 6 shows that for all six media studied, $S \approx 1$ does indeed correspond to the threshold background force level above which oil flows by background force alone without becoming trapped. The roughly linear dependence $V_{\text{oil}} \propto S$ in Figure 6 once $S > 1$ is simply a

of Gunstensen and Rothman (1993), who used a 3D lattice-Boltzmann model to study the flow of unconnected ganglia under steady forcing conditions. To determine the stimulation number S at each
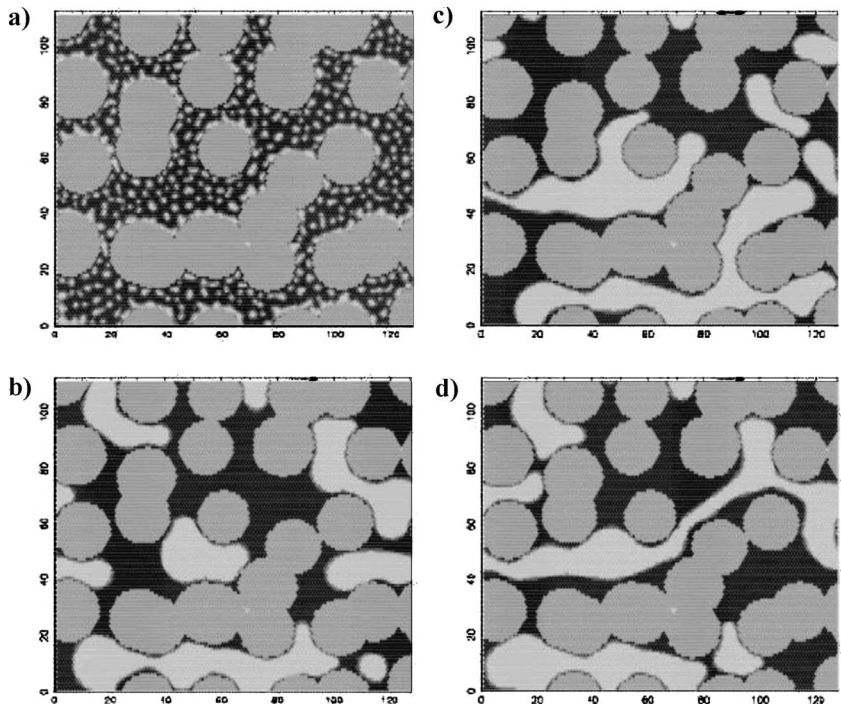

Figure 3. Snapshots during the four stages of the seismic-stimulation simulation. The fluid flow is from left to right. Solid grains are shown as gray, oil as light gray, and water as black. (a) The initial phase separation. (b) Force F_0 has caused the droplets to get stuck, and there is no flow of oil. (c) The stimulation is turned on $F_a > 0$, and the droplets coalesce. (d) A new steady state emerges as $F_a = 0$. There is now a flow through the system-spanning droplet.
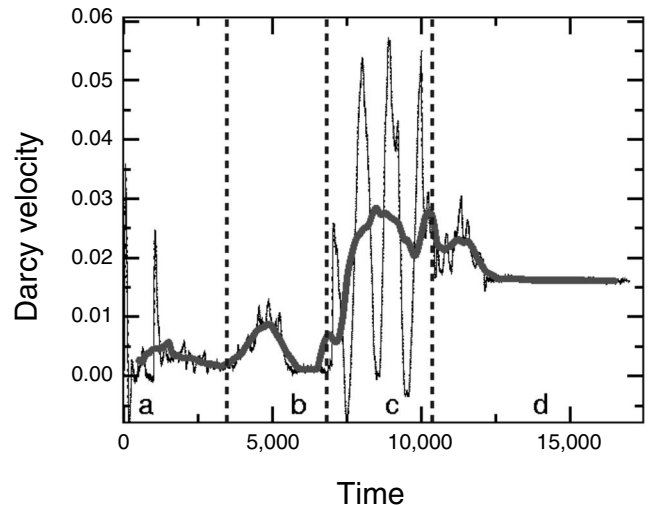

Figure 4. The spatially averaged Darcy velocity in the system as a function of simulation time (in units of the time step) corresponding to the geometry and flow shown in Figure 3. Each of the distinct time intervals defined in Figure 3 and denoted with a through d are separated by vertical dashed lines. The thin curve is the instantaneous velocity, and the thick curve is a running average over a time window
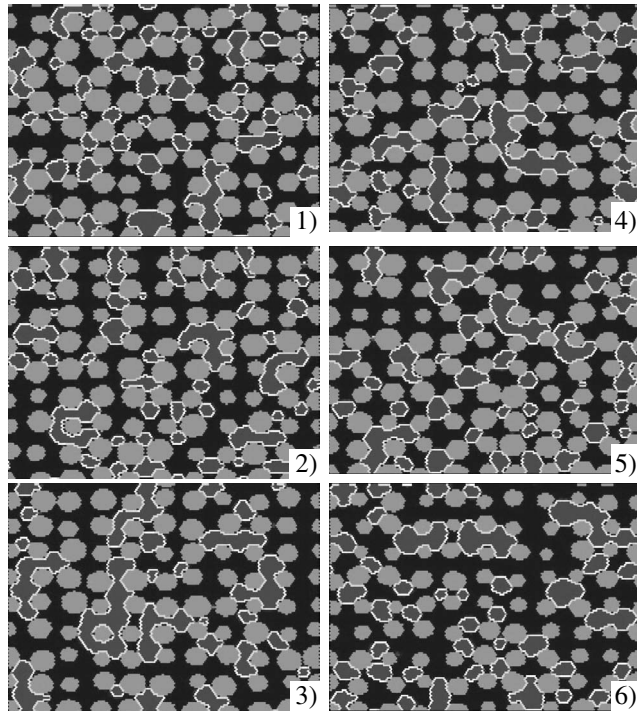
Figure 5. The six porous media studied at $N = 128$ resolution. Light gray = solid grains; black = wetting water; dark gray = nonwetting oil; white = boundary points surrounding the oil patches. All snapshots here are taken just after oil and water separation has occurred and prior to macroscopic forcing. All simulations are performed with one-third of the pore space occupied by oil and two-thirds occupied by water. Porosities and permeabilities (lattice units) for the six materials shown are $\phi_1 = 0.61$, $k_1 = 0.18$; $\phi_2 = 0.63$, $k_2 = 0.23$; $\phi_3 = 0.64$, $k_3 = 0.24$; $\phi_4 = 0.61$, $k_4 = 0.20$; $\phi_5 = 0.64$, $k_5 = 0.25$; and $\phi_6 = 0.71$, $k_6 = 0.42$.
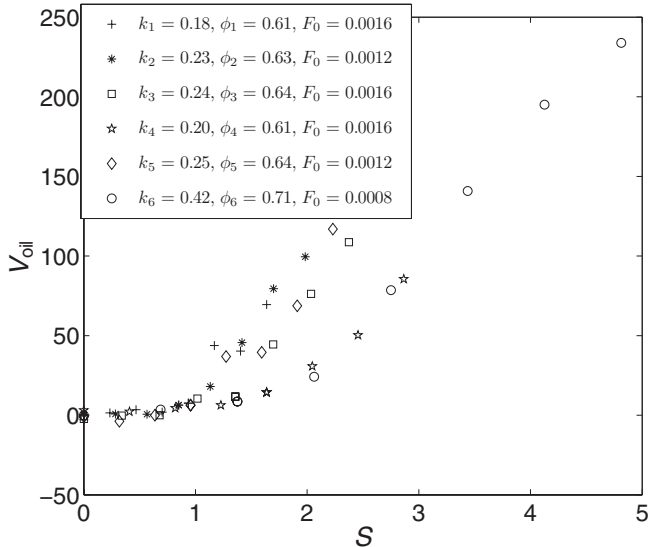
Figure 6. Specific oil volume V_{oil} as a function of the stimulation number S (related to applied force level) for the six porous media shown in Figure 5. The background forcing levels F_{oc} (in lattice Boltzmann units) are the critical values for each material at which trapped oil first becomes mobilized and correspond approximately

level of applied force F_o, it is necessary to numerically measure the average length h of the oil ganglia found in each system.

The same experiments are performed next with the inclusion of three cycles of seismic stimulation between time steps 9000 and 12,000, with $F_a/F_o = 1$. Figure 7 illustrates the result for two of the six materials, but similar results hold for all six. Stimulation is seen to enhance total oil produced during the run, even though the seismically coalesced bubbles cannot form system-spanning streams. If stimulation were applied for more than only three time-harmonic cycles, enhancement would have been greater.

A better way to see the effect of stimulation on oil production is to monitor (as in Figure 4) the average Darcy flow throughout the system $\bar{j}_{oil}$ as a function of time. Note that $\bar{j}_{oil}$ corresponds to the average flux of oil volume across each vertical slice of a system and thus is equivalent to the average rate of oil production throughout the system.

Figure 8 shows $\bar{j}_{oil}$ for the six systems at each time step of a production run with an additional 1000-time-step running average applied to see the net effect of each stimulation cycle. Solid symbols denote average production-rate histories without stimulation applied, and open symbols indicate those with the three cycles of stimulation. Although oil production drops back to almost zero after stimulation is turned off, net oil production is enhanced greatly during stimulation. Again, when the oil does not form system-spanning streams (as in this example), stimulation must be applied continuously to maintain enhanced production.

Mobilization and coalescence of trapped bubbles can occur only if the oil bubbles are moved a significant distance in a wave period compared with pore length. To quantify this condition, we carry out simulations with different T values. Recall that T is the ratio of the pore-length scale ℓ to the fluid displacement resulting from acoustic oscillations. This suggests that when $T > 1$, stimulation ceases to have an effect. In Figure 9, total produced oil is plotted as a function of T, and indeed, a critical T is observed around the value of one. Finite oil production for $T > 1$ results from both the initial displacement that occurs before stimulation is applied (stages a and b of Figure 4) and the fact that not all oil becomes trapped completely in the steady state prior to stimulation.
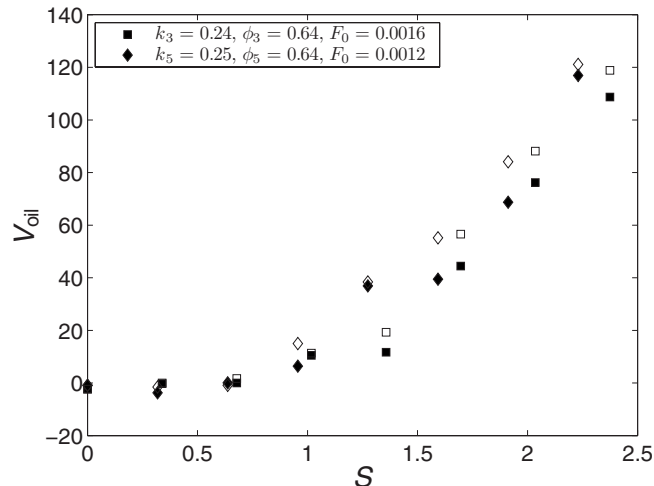

Figure 7. Specific oil volume V_{oil} that results with three time periods of stimulation applied (open symbols) and without any stimulation applied (solid symbols) for two of the six materials. Similar results hold for all six materials studied (plotting all six materials results in

In Figure 10, the specific volume V_{oil} is plotted as a function of F_a/F_o. In these simulations, F_o was kept constant at the value indicated in the figure, whereas F_a was increased. For all six materials, the value of $1/S - 1$ was between one-half and one. Thus, the stimulation criterion of $F_a/F_o > 1/S - 1$ is seen to be satisfied at least approximately. This is seen perhaps more clearly in Figure 11, in which the spatially averaged oil flux in the simulation cell $\bar{j}_{oil}$ is time-aver-

aged over the three cycles of applied stimulation and plotted as a function of F_a/F_o. If the bubbles remain trapped, they do not contribute to this averaged velocity, so the steady increase in average oil velocity with increasing F_a/F_o demonstrates that stimulation has a strong mobilization effect while it is turned on. Again, there is a finite oil velocity even when $F_a = 0$ because not all of the oil is trapped completely at the level of background force F_o used.

Figure 8. Average oil flux $\bar{j}_{oil}$ in each of the six systems with an additional 1000-time-step running average applied over the entire 18,000 time steps of the production runs. Solid symbols indicate that no stimulation was applied. Open symbols represent when three cycles of stimulation are applied between time steps 9000 and 12,000 with $F_a = F_0$ and F_0 given in the legend, which are the same values as the F_{0c} in Figure 6. Significant enhancement in the rate of oil production is observed for all six materials during stimulation.
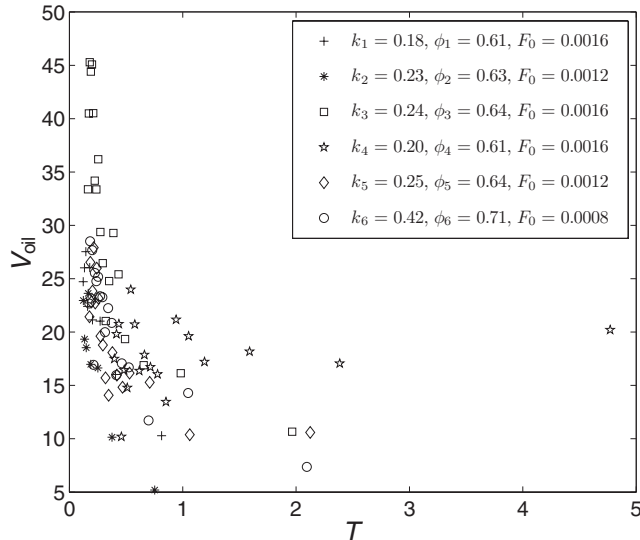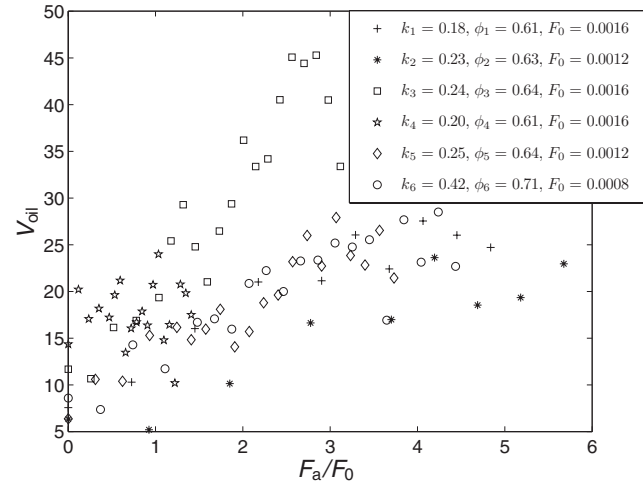

Figure 10. Total volume displacement of oil as a function of F_a/F_o when $0 < 1/S - 1 < 1$ for each of the six materials.

Figure 9. Specific oil volume V_{oil} as a function of the dimensionless frequency T defined by equation 16 when $S \approx 1/2$. At the lower frequencies corresponding to $T < 1$, one can see an enhanced level of oil production because stimulation has enough time in each cycle to
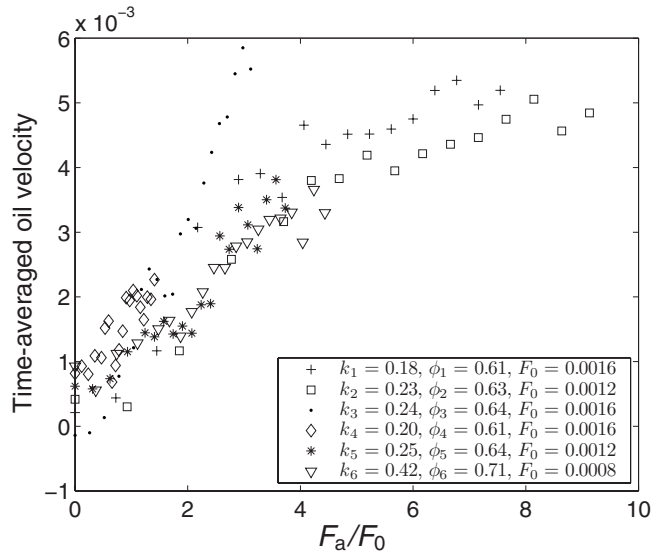

Figure 11. Oil velocity averaged over three cycles of applied stimulation when $T = 1/4$ and with F_o fixed to the values in the insert. In all six cases, $0 < 1/S - 1 < 1$, and thus these results are consistent with the stimulation criterion that oil becomes mobilized when $F_a/F_o > 1/S - 1$. If trapped oil were not liberated in each cycle, the

CONCLUSIONS

The main message of this study is supported strongly by numerical simulations: Seismic stimulation will mobilize trapped oil, thus increasing oil production when two dimensionless criteria are met. The first condition is the static-force requirement that when a seismic wave pushes on a trapped oil bubble, the radius of curvature of the downstream meniscus of the bubble is reduced sufficiently to get through the pore-throat constriction that is blocking its downstream progress. The second condition is the dynamic requirement that in a cycle of the time-harmonic stimulation, the meniscus has enough time to advance through the constriction before the seismic force changes direction and begins to push the meniscus upstream.

These two conditions can be achieved by using sufficiently large stimulation amplitudes and sufficiently small stimulation frequencies. Interestingly, when the stimulation force is modeled as that from a seismic wave and if seismic strain is independent of frequency, we predict that F_a increases linearly with frequency, although T becomes independent of frequency. Of course, the imposed seismic strain from different seismic sources working at different frequencies need not be the same. Further, in the field, the strain of a wave always is reduced at higher frequencies by seismic attenuation. Thus, there are many practical trade-offs to consider when choosing which source to work with and at what frequency.

Our main numerical results pertained to lower oil-volume fractions for which the stimulation-induced coalescence of bubbles did not result in a continuous stream of oil spanning the flow cell under study. At slightly larger oil-volume fractions, stimulation can form connected streams of oil that span the flow cell, thus creating an even larger oil-production effect.

Further numerical studies should be performed that (1) take simulations from two to three dimensions, (2) work with more grains in each flow cell, (3) apply stimulation for many hundreds or more of seismic wave periods, and (4) use alternative methods to simulate the way oil becomes trapped in the system in the first place. As an example of this last point, one might wish to start with a large volume fraction of oil in the system and perform an imbibition experiment until the advancing water front forms a percolating backbone. The oil that remains might be stuck only marginally and thus would be more susceptible to seismic stimulation.

To finish, we conjecture on the changes to be expected when simulations are taken to three dimensions, in which a greater number of junctions and oil branchings can occur that likely will result in a larger number of marginally stuck fingers of oil. On the other hand, the Rayleigh instability (an effect confined to three dimensions) will tend to break up larger ganglia into smaller ones, particularly when the solid is wetted by water, as in our simulations. In this case, the stimulation will need to be applied repeatedly to continuously remobilize and coalesce the oil droplets. Note that there is no intrinsic difficulty in performing the lattice-Boltzmann simulations in three dimensions. It is mainly a matter of applying a larger computational effort. Finally, in three dimensions, porosities can be reduced to those in real rocks because pore space remains connected across a sample even as porosity approaches zero.

ACKNOWLEDGMENTS

APPENDIX A

THE GASSMANN RELATIONS

An isotropic porous material has a compressional response governed by three elastic constants defined as

$$K_d = -\left(\frac{\delta P_c}{\delta V/V_o}\right)_{\delta p_f = 0}, \tag{A-1}$$

$$K_u = -\left(\frac{\delta P_c}{\delta V/V_o}\right)_{\nabla \cdot \mathbf{q} = 0}, \tag{A-2}$$

$$\text{and } B = -\left(\frac{\delta p_f}{\delta P_c}\right)_{\nabla \cdot \mathbf{q} = 0}, \tag{A-3}$$

where δP_c is the change in the confining pressure applied to the porous sample and where conditions $\delta p_f = 0$ and $\nabla \cdot \mathbf{q} = 0$ correspond to drained and undrained, respectively. At seismic frequencies, Pride (2005) shows that the strain response is effectively undrained; i.e., $\nabla \cdot \mathbf{q} = 0$ even though $\mathbf{q} \neq 0$.

With the drained (or dry) bulk modulus K_d taken as a known constant and assuming that the grains are uniform and isotropic, Gassmann (1951) shows how the undrained bulk modulus K_u and Skempton's coefficient B depend on K_d, porosity ϕ, solid grain modulus K_s and fluid modulus K_f,

$$B = \frac{1/K_d - 1/K_s}{1/K_d - 1/K_s + \phi(1/K_f - 1/K_s)}, \tag{A-4}$$

$$K_u = \frac{K_d}{1 - B(1 - K_d/K_s)}. \tag{A-5}$$

As the bulk modulus of the fluid becomes small compared with either K_d or K_s, one obtains

$$B \approx \frac{K_f}{\phi K_d}\left(1 - \frac{K_d}{K_s}\right) \quad \text{as } K_f \to 0, \tag{A-6}$$

which is meant to provide insight to the nature of B when some gas is present in the system.

Pride et al. (2004) showed that in the low-frequency (seismic-band) limit of interest here and when immiscible patches of oil and water are in the pores at volume fractions v_{oil} and v_{water}, the effective Skempton's coefficient becomes

$$\frac{1}{B} = \frac{v_{\text{oil}}}{B_{\text{oil}}} + \frac{v_{\text{water}}}{B_{\text{water}}}. \tag{A-7}$$

When using the monomineral result of Gassmann (1951), this is exactly equivalent to working with an effective fluid bulk modulus of

$$\frac{1}{K_f} = \frac{v_{\text{oil}}}{K_{\text{oil}}} + \frac{v_{\text{water}}}{K_{\text{water}}} \tag{A-8}$$

APPENDIX B

NEGLECTING COMPRESSIONAL CHANGES CAUSED BY THE WAVE

As a compressional wave squeezes a cell, the fact that water is typically less compressible than oil means that some water will tend to displace into pore space that initially was occupied by oil so that fluid pressures remain in quasi-static equilibrium at the low frequencies excited by the seismic source. For example, crude oil might have a bulk modulus of 2.0 GPa at 1-km depth, whereas pore water might have a modulus of 2.5 GPa (e.g., Batzle and Wang, 1992). Such compressional-induced displacement of the menisci is not being modeled in the present paper. Order-of-magnitude estimates now are provided for menisci displacements resulting from this compressional effect compared with displacements from the Darcy flux induced by F_a. These estimates will be made assuming that surface tension is negligible because allowing for finite surface tension will reduce each type of displacement an equivalent amount.

First, the low-frequency (seismic-band) results of Pride et al. (2004) can be used to estimate the quantity ζ_{int}, which is the volume of fluid that passes from pores initially occupied by oil to pores initially occupied by water, as normalized by the volume of the flow cell under consideration. The average "compression-induced" meniscus displacement δ_ζ is obtained by combining equations 8, 47-52, and 69 of Pride et al. (2004) to give

$$\delta_\zeta = \frac{V\zeta_{int}}{S_m} = v_{water}v_{oil}\left(\frac{1}{B_{oil}} - \frac{1}{B_{water}}\right)\left(\frac{K_u}{K_d} - 1\right)\frac{V}{S_m}\theta.$$

(B-1)

In a flow cell of volume V, a fraction v_{oil} of the porous material is saturated with oil, a fraction v_{water} is saturated with water (with $v_{water} + v_{oil} = 1$), and there is a total surface area S_m of the menisci that separate oil-saturated from water-saturated patches. In addition, K_d is the drained bulk modulus, and one always has that $K_u > K_d$.

Next, the Darcy filtration velocity q_ω created by seismic force F_a is given by $q_\omega = (k/\eta_f)F_a$ so that on using equation 6, the relative fluid-solid displacement δ_q induced by F_a is

$$\delta_q = \frac{1}{-i\omega\phi}q_\omega = \frac{\rho_f c_p k}{\eta_f \phi}\left(1 + \frac{\rho}{\rho_f}\frac{B}{1 + 4G/3K_u}\right)\theta,$$

(B-2)

where ϕ is porosity.

For a 20% porosity sandstone 10% occupied by crude oil and having a drained bulk modulus of $K_d = 12$ GPa, the Gassmann relations given in Appendix A predict that $B_{oil} = 0.37$, $B_{water} = 0.40$, and $K_u = 16$ GPa. If we estimate δ_q using water properties and take $V/S_m = 10^{-2}$ m along with $k = 10^{-12}$ m^2, we find the order-of-magnitude estimate that

$$\frac{\delta_\zeta}{\delta_q} = 10^{-3}.$$

(B-3)

These estimates suggest that neglecting the compressional effect is a reasonable approximation in a first modeling of seismic stimulation. This is especially true for more permeable formations where seismic stimulation has a chance of working.

and upstream menisci trapped on pore-throat barriers. The compression effect will cause the downstream and upstream menisci to displace in opposite directions, thus moving one meniscus closer to getting through its barrier while moving the other farther away, with a net effect that perhaps is canceling. Displacements induced by F_a will push upstream and downstream menisci in the same direction, simultaneously bringing them both closer to moving through their respective barriers.

A final compressional effect perturbing flow at a distant cell is the change in permeability created by a compressional wave. Pride (2005) has derived an expression that details how much permeability k changes when pressure is applied to a flow cell. In the present context, that expression can be written as $\delta k/k = a\theta$. Here, θ is the compressional wave strain. The dimensionless material property a has a complicated dependence on the elastic moduli and pore-space tortuosity that will not be written out here but that is approximately of order 1 in amplitude. Because typically $\theta < 10^{-6}$ a few meters from the seismic source, flow perturbation resulting from changes in permeability is less than one part in a million, which is entirely negligible compared with perturbations caused by F_a.

APPENDIX C

THE LATTICE-BOLTZMANN MODEL

We simulate the two-phase flow using a slightly simplified version of the lattice-Boltzmann model introduced by Gunstensen at al. (1991) and Gunstensen and Rothman (1993). The simplification consists of replacing the multiple relaxation times in the lattice-Boltzmann operator by a single relaxation time $1/\lambda$. We use a lattice-BGK algorithm (Qian et al., 1992). For completeness, we briefly review the model here.

The oil and water are represented by red and blue fluid masses, R_i and B_i, respectively. These masses exist on the sites of a triangular lattice. On each site, there are six directions or channels labeled by index i in which masses can propagate. This is illustrated in Figure C-1.

Every time step $t \rightarrow t + 1$ contains two steps. First, the masses are propagated to their neighboring sites $R_i(\mathbf{x}) \rightarrow R_i(\mathbf{x} + \mathbf{c}_i)$ and $B_i(\mathbf{x}) \rightarrow B_i(\mathbf{x} + \mathbf{c}_i)$, and then the masses are subjected to a local update, which usually is referred to as a collision step. Taking the lattice
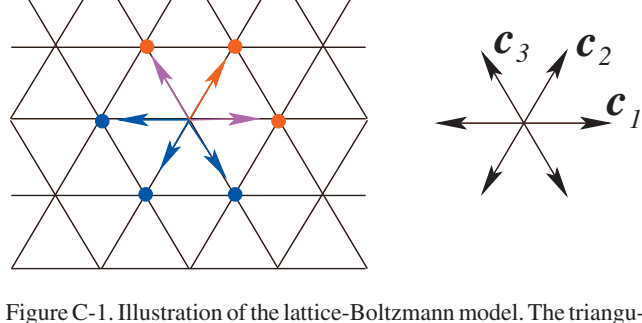

Figure C-1. Illustration of the lattice-Boltzmann model. The triangular lattice supports a population of red and blue particle masses distributed over the six spatial directions. Arrows represents amount and color of the mass in each direction, and dots represent the total mass on the corresponding sites. Magenta arrows (directions $+ \mathbf{c}_1$ and $+ \mathbf{c}_3$ in the figure) represent a mix of color, i.e., a finite value of

sites to have coordinates $(\mathbf{x},t)$ at the discrete time t, we can write the corresponding evolution equation of the masses as

$$R_i(\mathbf{x} + \mathbf{c}_i, t + 1) = R_i(\mathbf{x},t) + \Delta R_i$$

and

$$B_i(\mathbf{x} + \mathbf{c}_i, t + 1) = B_i(\mathbf{x},t) + \Delta B_i, \qquad (\text{C-1})$$

where ΔB_i and ΔR_i represent the change in the masses that occur on the lattice sites at every time step. These changes conserve the individual site color masses and the site momentum. These local conservation laws are the underlying reason for macroscopic hydrodynamic behavior.

The first part of the collision step guarantees hydrodynamic behavior of the system as viewed by a color-blind observer because it deals only with the summed masses $N_i = R_i + B_i$. This part can be written as

$$N_i \rightarrow N_i + \Delta N_i, \qquad (\text{C-2})$$

where

$$\Delta N_i = \lambda(N_i - N_i^{eq}(\rho,\mathbf{u})) + \frac{1}{3}\mathbf{c}_i \cdot \mathbf{F}, \qquad (\text{C-3})$$

where λ is a relaxation parameter, $\mathbf{F}$ will be shown to be the external body force, and the equilibrium distributions N_i^{eq} are the values of N_i after all gradients of the hydrodynamic mass and momentum densities

$$\rho(\mathbf{x},t) = \sum_{i=1}^{6} N_i(\mathbf{x},t)$$

$$\text{and } \rho\mathbf{u}(\mathbf{x},t) = \sum_{i=1}^{6} N_i(\mathbf{x},t)\mathbf{c}_i \qquad (\text{C-4})$$

have vanished. These equilibrium densities can be chosen, and we choose them to be

$$N_i^{eq}(\rho,\mathbf{u}) = \frac{\rho}{6}(1 + 2\mathbf{c}_i \cdot \mathbf{u} + 4((\mathbf{c}_i \cdot \mathbf{u})^2 - |\mathbf{u}|^2/2)). \qquad (\text{C-5})$$

It can be shown that $\sum_{i=1}^{6} N_i^{eq} = \rho$ and $\sum_{i=1}^{6} N_i^{eq}\mathbf{c}_i = \rho\mathbf{u}$. Hence, this choice guarantees that in the long-wavelength, low-Mach-number limit, the mass and momentum densities satisfy the following Navier-Stokes equation (Rothman and Zaleski, 1997):

$$\nabla \cdot \mathbf{u} = 0$$

$$\rho\frac{d\mathbf{u}}{dt} = \nabla P(\rho) + \eta\nabla^2\mathbf{u} + \mathbf{F}, \qquad (\text{C-6})$$

where pressure $P = \rho/2$ and viscosity

$$\eta = -\frac{\rho}{4}\left(\frac{1}{2} + \frac{1}{\lambda}\right). \qquad (\text{C-7})$$

For $0 < \eta < \infty$, we must have $-2 < \lambda < 0$. The time derivative in equation 6 is the total derivative given by $d/dt = \partial/\partial t + \mathbf{u} \cdot \nabla$.

and surface tension consists of two steps. First, there is a redistribution of the N_is that increases the mass in the direction perpendicular to the fluid interfaces

$$N_i \rightarrow N_i' = N_i + A|\mathbf{f}|\left(\frac{(\mathbf{c}_i \cdot \mathbf{f})^2}{|\mathbf{f}|^2} - \frac{1}{2}\right), \qquad (\text{C-8})$$

where A is a parameter and the color gradient $\mathbf{f}$ is defined as

$$\mathbf{f} = \sum_{j=1}^{6} \mathbf{c}_j \sum_{i=1}^{6} (R_i(\mathbf{x} + \mathbf{c}_j) - B_i(\mathbf{x} + \mathbf{c}_j)). \qquad (\text{C-9})$$

It can be shown that this step does not alter the site mass or momentum. Finally, the colored mass is redistributed so that the red (blue) mass is sent in the direction toward red (blue) neighbors under the constraints of color conservation and $R_i + B_i = N_i'$. This recoloring step, a sort of inverse diffusion, maintains the sharpness of the interfaces. The result of this recoloring step is illustrated in Figure C-1. It is shown (Gunstensen et al., 1991) that surface tension σ takes the form

$$\sigma = -\frac{9A\rho}{\lambda}f(\beta), \qquad (\text{C-10})$$

where β is the angle between the fluid interface and a lattice direction. The (slight) anisotropy of the surface tension is measured by $f(\beta)$. It is shown by Gunstensen et al. (1991) that $0.9 < f(\beta) < 1.1$, and in the present context, we shall ignore this anisotropy, which will create somewhat noncircular bubbles. The validity of the above surface tension formula can be checked by measuring the pressure difference between the inside and outside of a drop, and the agreement is excellent (Gunstensen et al., 1991).

To simulate the viscosity contrast that exists between the two phases, we take the viscosity to be

$$\eta = (\eta_r\rho_r(\mathbf{x},t) + \eta_b\rho_b(\mathbf{x},t))/\rho(\mathbf{x},t), \qquad (\text{C-11})$$

where η_r (η_b) is the viscosity of the red (blue) phase, $\rho_r = \Sigma_i R_i(\mathbf{x},t)$, and $\rho_b = \Sigma_i B_i(\mathbf{x},t)$.

The solid surfaces should cause a no-slip boundary condition for the fluid flow along them. In the simulations, this is achieved to a good approximation by reversing the particle populations there, i.e., on the solid sites $\mathbf{x}$, $R_i(\mathbf{x},t) \rightarrow R_{i+3}(\mathbf{x},t)$ and likewise for the B_is at every time step.

The wetting properties of the solid are incorporated by giving the solid sites a color. If this color is blue (water), then water will wet the solid completely, and the contact angle will be zero degrees. If it is a mix of red and blue, there will be a finite contact angle. The color of the solid sites enters into the computation of only $\mathbf{f}$.

REFERENCES

Archie, G. E., 1942, The electrical resistivity log as an aid in determining some reservoir characteristics: Transactions of the American Institute of Mining, Metallurgical and Petroleum Engineers, **146**, 54–62.

Batzle, M., and Z. Wang, 1992, Seismic properties of pore fluids: Geophysics, **57**, 1396–1408.

Beresnev, I., and P. Johnson, 1994, Elastic-wave stimulation of oil production: A review of methods and results: Geophysics, **59**, 1000–1017.

Beresnev, I. A., R. D. Vigil, W. Li, W. D. Pennington, R. M. Turpening, P. P. Iassonov, and R. P. Ewing, 2005, Elastic waves push organic fluids from reservoir rock: Geophysical Research Letters, **32**, L13303.

Beresnev, I., 2006, Theory of vibratory mobilization of nonwetting fluids en-

Biot, M. A., 1956, Theory of propagation of elastic waves in a fluid-saturated porous solid. I. Low-frequency range: Journal of the Acoustical Society of America, **28**, 168–178.

Chandrasekhar, S., 1961, Hydrodynamic and hydromagnetic stability: Dover.

Gassmann, F., 1951, Über die Elastizität poröser Medien: Vierteljahrsschrift der Naturforschenden Gesellschaft, **96**, 1–23 (in German).

Gunstensen, A. K., and D. H. Rothman, 1993, Lattice-Boltzmann studies of two-phase flow through porous media: Journal of Geophysical Research, **98**, 6431–6441.

Gunstensen, A. K., D. H. Rothman, S. Zaleski, and G. Zanetti, 1991, A lattice-Boltzmann model of immiscible fluids: Physical Review A, **43**, 4320–4327.

Hilpert, M., G. Jirka, and E. Plate, 2000, Capillary-induced resonance of oil blobs in capillary tubes and porous media: Geophysics, **65**, 874–883.

Hilpert, M., 2007, Capillary-induced resonance of oil blobs in porous media: Analytical solutions, lattice-Boltzmann modeling, and blob mobilization: Journal of Colloidal and Interface Science, **309**, 493–504.

Iassonov, P., and I. A. Beresnev, 2003, A model of enhanced fluid percolation in porous media by application of low-frequency elastic waves: Journal of Geophysical Research, **108**, no. B3, ESE 2-1, doi: .

Li, W., R. Vigil, I. Beresnev, P. Iassonov, and R. Ewing, 2005, Vibration-induced mobilization of trapped oil ganglia in porous media: Experimental validation of a capillary-physics mechanism: Journal of Colloidal and Interface Science, **289**, 193–199.

Pride, S. R., J. G. Berryman, and J. M. Harris, 2004, Seismic attenuation due to wave-induced flow: Journal of Geophysical Research, **109**, no. B1, B01201, doi: .

Pride, S. R., 2005, Relationships between seismic and hydrological properties, *in* Y. Rubin, and S. Hubbard, Hydrogeophysics: Springer, 253–290.

Qian, Y., D. D'Humières, and P. Lallemand, 1992, Lattice BGK models for Navier-Stokes equation: Europhysical Letters, **17**, 479–484.

Roberts, P., A. Sharma, V. Uddameri, M. Monagle, D. Dale, and L. Steck, 2001, Enhanced DNAPL transport in a sand core during dynamic stress stimulation: Environmental Engineering Science, **18**, 67–79.

Rothman, D., and S. Zaleski, 1997, Lattice-gas cellular automata: Simple models of complex hydrodynamics: Cambridge University Press.

Skempton, A. W., 1954, The pore-pressure coefficients A and B: Geotechnique, **4**, 143–147.